MOX-Report No. 76/2021

A PDE-regularized smoothing method for space-time data over manifolds with application to medical data

Ponti, L.; Perotto, S.; Sangalli, L.M.

MOX, Dipartimento di Matematica
Politecnico di Milano, Via Bonardi 9 - 20133 Milano (Italy)

mox-dmat@polimi.it http://mox.polimi.it

A PDE-regularized smoothing method for space-time data over manifolds with application to medical data

Luca Ponti[♯], Simona Perotto[*], Laura M. Sangalli[*]

November 19, 2021

[♯] Politecnico di Milano
Piazza L. da Vinci 32, I-20133 Milano, Italy
[*]MOX– Dipartimento di Matematica, Politecnico di Milano
rufusponti@gmail.com,{simona.perotto,laura.sangalli}@polimi.it

Abstract

We propose an innovative statistical-numerical method to model spatio-temporal data, observed over a generic two-dimensional Riemanian manifold. The proposed approach consists of a regression model completed with a regularizing term based on the heat equation. The model is discretized through a finite element scheme set on the manifold, and solved by resorting to a fixed point-based iterative algorithm. This choice leads to a procedure which is highly efficient when compared with a monolithic approach, and which allows us to deal with massive datasets. After a preliminary assessment on simulation study cases, we investigate the performance of the new estimation tool in practical contexts by dealing with neuroimaging and hemodynamic data.

1 Introduction

This work proposes a statistical-numerical methodology to analyze spatio-temporal data measured on general two-dimensional Riemanian manifold domains. These kinds of data are very common in diverse contexts, from Engineering to Applied Sciences. In an Engineering design process, for instance, it is standard to study time- as well as space-varying quantities of interest observed over the surface of a three-dimensional prototype in order to optimize the design pipeline (e.g., the aerodynamic forces exerted on the surface of an airfoil, when dealing with the design of an airplane). In Environmental Science, it is of paramount importance to accurate model space-time data distributed over regions characterized by a complex orography, for example, in order to better understand the earth processes, or to control pollution or global climate changes, or to optimize the exploitation of natural resources. In this paper, we focus on some applications which arise from Life Science. Figure 1 refers to one of the analyzed contexts. The panel on the left shows the mesh approximating the cortical surface of a brain, on which the hemodynamic signal, induced

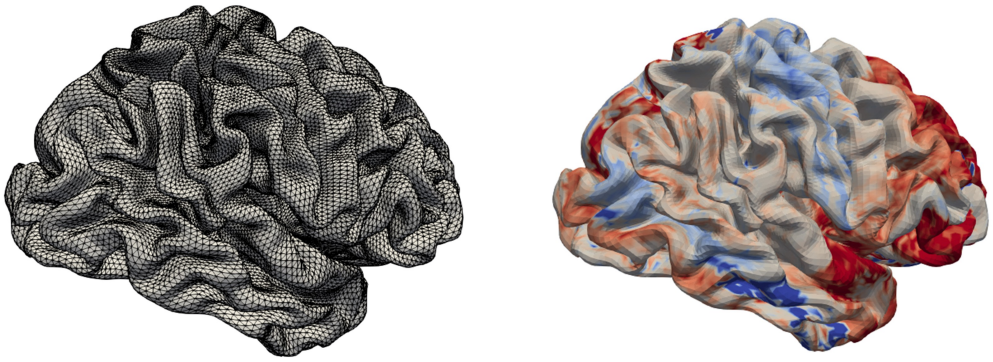

Figure 1: Neuroimaging signal on a cerebral cortex: triangular mesh modeling the cortical surface (left); fMRI signal associated with neuronal activity distributed over the cortex at a certain temporal instant (right).

by the neuronal activity on the cortical surface, shown in the right panel has been observed, at a certain time. Standard spatio-temporal techniques, that rely on the Euclidean distance, are not suited, in general, to handle data such as the ones in Figure 1. Due to folded geometry of the domain, such methods can yield highly inaccurate estimates, by incorrectly identifying as close, data locations that actually are far apart on the real geometry. Thus, values observed over two distinct gyri could be artificially linked each other, although, in practice, separated by a sulcus. As a consequence, in order to obtain accurate estimates on complex manifolds, it becomes mandatory to appropriately comply with the complex geometry of the domain.

The diversified demands characterizing a so large number of different application fields justify the strong interest for data analysis over two-dimensional Riemannian manifolds, both in the statistical and in the numerical literature. Nevertheless, the available methodologies are so far confined to special manifolds, such as spheres or sphere-like domains (see, e.g., [4, 5, 20, 21, 27, 28, 34] and the references therein), or to the spatial dimension only (see, e.g., [6, 7, 10, 11, 15, 17, 22, 35]).

The challenge tackled in this paper is consequently twofold, since dealing with space-time data over a general two-dimensional manifold. To this aim, we propose a computational procedure which belongs to, and further strongly advances, the class of Spatial Regression with PDE regularization (SR-PDE) methods reviewed in [31]. In particular, we adopt an estimation functional which combines a least-square data-fidelity criterion with a regularizing term based on the heat equation. The work is inspired by the regression model for spatial data over manifold domains considered in [15], as well as to the spatio-temporal model for planar domains proposed in [2]. In more detail, here we discretize the problem directly on the manifold instead of resorting to a conformal flattening of the domain as in [15]. This allows us to avoid the approximation error characterizing the flattening step. Moreover, we use an iterative fixed-point scheme to solve the discrete problem instead of the monolithic approach adopted in [2]. Such a choice ensures a highly computational ef-

ficiency, and makes it possible to handle massive datasets, such as those characterizing the applied problems mentioned above.
The paper is organized as follows. Section 2 introduces the proposed PDE-regularized spatio-temporal smoothing method. Section 3 details the discretization used to solve the estimation problem, by distinguishing between the monolithic approach and the new fixed point-based algorithm. Section 4 shows the good performances of the new method through simulation study cases, whereas Section 5 focuses on two in Life Science applications, by considering neuroimaging data and the study of cerebral aneurysms. Finally, Section 6 outlines possible directions for a future research.

2 Regression analysis with PDE regularization

We consider a two-dimensional Riemannian manifold, $\mathcal{M} \subset \mathbb{R}^3$, with n data locations, $\{\mathbf{p}_i,\ i = 1, \ldots, n\}$, and a time window, $I = [0, T]$, with m temporal instants, t_1, t_2, $\ldots, t_m$, where $0 = t_1 < t_2 < \ldots < t_m = T$. We denote by z_{ij} the value of a real-valued random variable of interest, when observed at the space-time location $(\mathbf{p}_i, t_j)$, for $i = 1, \ldots, n$ and $j = 1, \ldots, m$. We assume that the random variable coincides with a noisy observation of a smooth function, $f : \mathcal{M} \times [0, T] \longrightarrow \mathbb{R}$, according to the model

$$z_{ij} = f(\mathbf{p}_i, t_j) + \epsilon_{ij} \quad \text{for } i = 1, \ldots, n,\ j = 1, \ldots, m, \tag{1}$$

where ϵ_{ij} are independent measurement errors characterized by a zero mean and a finite variance. Additionally, we assume that f is twice continuously differentiable in space and continuously differentiable in time.

Our goal is to estimate the space-time field f in (1) in the presence of an a priori knowledge on the phenomenon of interest. In particular, as in [2], we assume that the problem under study can be described in terms of a time-dependent law, represented by a parabolic partial differential equation (PDE). The problem-specific information may include also the boundary conditions (B.C.) when $\mathcal{M}$ is an open manifold, and the initial condition (I.C.), that model the behaviour of the field f at the boundary, $\partial\Omega \times \{0, T\}$, of the space-time domain of interest.
We propose to estimate f by minimizing the regularized sum of squared function errors

$$J_\lambda(f) = \sum_{i=1,\ldots,n} \sum_{j=1,\ldots,m} \left[z_{ij} - f(\mathbf{p}_i, t_j)\right]^2 + \lambda \int_0^T \int_{\mathcal{M}} \left(\Delta_{\mathcal{M}} f - \frac{\partial f}{\partial t}\right)^2 d\mathbf{p}dt, \tag{2}$$

where $\Delta_{\mathcal{M}}$ is the Laplace-Beltrami operator defined on $\mathcal{M}$, λ is a positive smoothing parameter, and $(\mathbf{p}, t)$ denotes the generic space-time coordinate varying in $\mathcal{M} \times I$.
Functional J_λ formalizes a trade-off between a data fitting and a model fidelity criterion. On the one hand, the sum of the squared function errors pushes the solution to the minimization problem, denoted by $\hat{f}$, close to the observed data z_{ij} when evaluated at the space-time locations $(\mathbf{p}_i, t_j)$. On the other hand, the penalizing term controls the regularity, in space and time, of $\hat{f}$. In particular, the Laplace-Beltrami operator generalizes the standard Laplacian to the case of a function defined over a manifold, by providing a

simple measure of the local curvature of such a function. Operator $\Delta_{\mathcal{M}}$ is invariant with respect to Euclidean transformations (rotations, translations and reflections) of the spatial coordinates. This ensures that the smoothness of $\hat{f}$ does not depend on the orientation of the coordinate system we adopt or of the domain. Finally, parameter λ tunes the trade-off between data fidelity and regularity, so that the higher the parameter λ, the more regular the estimate; vice versa, the lower the parameter λ, the closer the fit to the observed data.
Now, we establish the function setting associated with the minimization of functional J_λ. With this aim, we introduce the Sobolev space $H^k(\mathcal{M})$ of the functions, $u : \mathcal{M} \longrightarrow \mathbb{R}$, which belong to $L^2(\mathcal{M})$ together with the associated partial derivatives up to the order k ($L^2(\mathcal{M})$ coinciding with $H^0(\mathcal{M})$), and the space $L^2(0,T;H^k(\mathcal{M}))$ of the functions u defined over $(0,T)$ and taking values in $H^k(\mathcal{M})$, such that $\int_0^T \|u(t)\|^2_{H^k(\mathcal{M})} dt < +\infty$ [13]. It can be checked that the estimation problem

$$\text{find } \hat{f} \text{ such that } \hat{f} = \underset{f}{\operatorname{argmin}} \; J_\lambda(f) \tag{3}$$

is well-defined in the space $V_T^2(\mathcal{M})$, with

$$V_T^s(\mathcal{M}) = \left\{ v \in L^2(0,T;H^s(\mathcal{M}) \cap C^0(\mathcal{M})) : \frac{\partial v}{\partial t} \in L^2(0,T;L^2(\mathcal{M})) \text{ + B.C. and I.C.} \right\}, \tag{4}$$

$s \in \mathbb{N}^+$, and where, here and below, the space, $C^0(\mathcal{M})$, of the functions continuous on $\mathcal{M}$ has to be meant associated with the closure of $\mathcal{M}$ when $\mathcal{M}$ coincides with an open manifold. Moreover, boundary and initial conditions will be properly included in the definition of space $V_T^s(\mathcal{M})$, according to the specific problem at hand.

In this paper, we focus on the proposal of an efficient numerical approximation for the estimation problem (3). It turns out that the estimator $\hat{f}$ minimizing the cost functional J_λ in $V_T^2(\mathcal{M})$ satisfies the identity

$$\begin{aligned} &\sum_{i=1,\dots,n} \sum_{j=1,\dots,m} \hat{f}(\mathbf{p}_i,t_j) q(\mathbf{p}_i,t_j) + \lambda \int_0^T \int_{\mathcal{M}} \left(\Delta_{\mathcal{M}} \hat{f} - \frac{\partial \hat{f}}{\partial t} \right) \left(\Delta_{\mathcal{M}} q - \frac{\partial q}{\partial t} \right) d\mathbf{p} dt \\ = &\sum_{i=1,\dots,n} \sum_{j=1,\dots,m} q(\mathbf{p}_i,t_j) z_{ij} \end{aligned} \tag{5}$$

for any function $q \in V_T^2(\mathcal{M})$. Equation (5) can be rewritten as a system of coupled parabolic problems, by introducing a suitable auxiliary function g defined on $\mathcal{M}$ [15]. Thus, we look for the pair $(\hat{f}, g) \in V_T^1(\mathcal{M}) \times V_T^1(\mathcal{M})$, with $V_T^1(\mathcal{M})$ defined according to

(4), such that,

$$\begin{cases} \displaystyle\int_0^T \int_{\mathcal{M}} \nu\, g\, d\mathbf{p}dt + \int_0^T \int_{\mathcal{M}} \left(\nabla_{\mathcal{M}} \hat{f} \cdot \nabla_{\mathcal{M}} \nu + \frac{\partial \hat{f}}{\partial t} \nu \right) d\mathbf{p}dt = 0 \\ \displaystyle\sum_{i=1,\dots,n} \sum_{j=1,\dots,m} \hat{f}(\mathbf{p}_i, t_j) q(\mathbf{p}_i, t_j) - \lambda \int_0^T \int_{\mathcal{M}} \left(\nabla_{\mathcal{M}} g \cdot \nabla_{\mathcal{M}} q - \frac{\partial g}{\partial t} q \right) d\mathbf{p}dt \\ \displaystyle= \sum_{i=1,\dots,n} \sum_{j=1,\dots,m} q(\mathbf{p}_i, t_j) z_{ij}, \end{cases} \tag{6}$$

with $(\nu, q) \in V_T^1(\mathcal{M}) \times V_T^1(\mathcal{M})$, and where $\nabla_{\mathcal{M}}$ denotes the gradient operator associated with the manifold $\mathcal{M}$. We remark that the first problem in (6) coincides with a standard (forward) parabolic PDE, whereas the problem associated with g constitutes a backward parabolic PDE, since the time derivative and the diffusive term are characterized by an opposite sign. As a consequence, the initial condition $\hat{f}(\mathbf{p}, 0) = \tilde{f}_0$ is added to the first equation, while the ending condition $g(\mathbf{p}, T) = \tilde{g}_T$ completes the second PDE.
Concerning the conditions to be assigned on $\partial\Omega$, we will select the boundary data according to the test case at hand. In particular, the essential boundary conditions will be explicitly included in the definition of space $V_T^1(\mathcal{M})$.

Formulation (6) turns out to be instrumental in view of the discrete counterpart of problem (3). In particular, the numerical procedure proposed in the next section will be characterized by a considerable computational efficiency, thanks to the introduction of an ad-hoc iterative algorithm. This feature will allow us to handle massive datasets, typical of several applicative contexts.

3 Discretization of the estimation problem

This section represents the methodological core of the paper. We provide an improvement in terms of computational efficiency of the approach used in [2] to tackle system (6) in the simplified case of data distributed over a planar domain according to specific sampling designs (e.g., pointwise spatial/interval temporal data, areal spatial/pointwise temporal data, areal spatial/interval temporal data). The final goal is to finalize a handy and accurate procedure able to efficiently analyze considerable amount of space-time data, observed over general two-dimensional Riemannian manifold domains.

In particular, to approximate the system of parabolic PDEs in (6), we have to define a discretization both in space and time. To discretize the space, we introduce a conformal triangulation, $\mathcal{T}_h = \{K\}$, of the manifold $\mathcal{M}$, h being the characteristic mesh size. To discretize the time dependence, we consider a partition, $\tau_1 = 0 < \tau_2 < \ldots < \tau_M = T$, of the time window $(0, T]$ into $(M-1)$ subintervals, $(\tau_{k-1}, \tau_k]$, of length Δt, with $k = 2, \ldots, M$. For simplicity of exposition, we assume that the vertices of $\mathcal{T}_h$ exactly coincide with the data locations $\mathbf{p}_i$, and that the times when data are collected identify the time partition, so that $M \equiv m$ and $\tau_j \equiv t_j$ for $j = 1, \ldots, m$.

Then, we define the finite element space, $V_h^r(\mathcal{M}) = \left\{v_h \in C^0(\mathcal{M}) : v_h\big|_K \in \mathbb{P}^r(K), \forall K \in \mathcal{T}_h\right\}$, associated with the tessellation $\mathcal{T}_h$, where $\mathbb{P}^r(K)$ denotes the space of the polynomials of degree r defined on K. Notice that the (essential) boundary conditions characterizing space $V_T^1(\mathcal{M})$ are inherited by the discrete space $V_h^r(\mathcal{M})$.
We consider a Lagrangian basis $\mathcal{B} = \{\psi_1, \ldots, \psi_{N_\mathcal{T}}\}$ of the space $V_h^r(\mathcal{M})$, associated with the nodes $\boldsymbol{\xi}_1, \ldots, \boldsymbol{\xi}_{N_\mathcal{T}}$ of the triangulation, being $\dim(V_h^r(\mathcal{M})) = N_\mathcal{T}$ (we remind that the nodes are, in general, a super-set of the mesh vertices; only for linear finite elements ($r = 1$), the nodes exactly coincide with the vertices of $\mathcal{T}_h$). Thus, each function $v_h \in V_h^r(\mathcal{M})$ can be expressed in terms of this basis as $v_h(\mathbf{x}) = \sum_{i=1}^{N_\mathcal{T}} v_h(\boldsymbol{\xi}_i)\psi_i(\mathbf{x}) = \mathbf{v}^T\boldsymbol{\psi}(\mathbf{x})$, where vector $\boldsymbol{\psi}(\mathbf{x}) = [\psi_1(\mathbf{x}), \ldots, \psi_{N_\mathcal{T}}(\mathbf{x})]^T$ collects the $N_\mathcal{T}$ finite element basis functions at the generic point $\mathbf{x} \in \mathcal{M}$, while vector $\mathbf{v} = [v_h(\boldsymbol{\xi}_1), \ldots, v_h(\boldsymbol{\xi}_{N_\mathcal{T}})]^T \in \mathbb{R}^{N_\mathcal{T}}$ gathers the evaluation of function v_h at the $N_\mathcal{T}$ nodes.
In addition, if we define the vector $\mathbf{v}_n = [v_h(\mathbf{p}_1), \ldots, v_h(\mathbf{p}_n)]^T \in \mathbb{R}^n$ of the evaluations of function v_h at the n data locations, $\mathbf{p}_1, \ldots \mathbf{p}_n$, the matrix $\Psi = (\boldsymbol{\psi}^T(\mathbf{p}_1), \ldots, \boldsymbol{\psi}^T(\mathbf{p}_n)) \in \mathbb{R}^{n \times N_\mathcal{T}}$ of the evaluations of the basis functions at the same points, we can relate vectors $\mathbf{v}$ and $\mathbf{v}_n$ via the equality $\mathbf{v}_n = \Psi\mathbf{v}$. In particular, for $r = 1$, matrix Ψ reduces to the identity matrix, $I \in \mathbb{R}^{n \times n}$, and $\mathbf{v} \equiv \mathbf{v}_n$.
By extending the notation above, we denote by

$$\mathbf{v}^k = [v_h(\boldsymbol{\xi}_1, t_k), \ldots, v_h(\boldsymbol{\xi}_{N_\mathcal{T}}, t_k)]^T \in \mathbb{R}^{N_\mathcal{T}}, \qquad \mathbf{v}_n^k = [v_h(\mathbf{p}_1, t_k), \ldots, v_h(\mathbf{p}_n, t_k)]^T \in \mathbb{R}^n \tag{7}$$

the vectors gathering the values taken at time t_k by v_h at the finite element nodes and at the data locations, respectively so that $\mathbf{v}_n^k = \Psi\mathbf{v}^k$, where, for $r = 1$ it holds $\mathbf{v}^k \equiv \mathbf{v}_n^k$ with $k = 1, \ldots, m$, being $\boldsymbol{\xi}_i \equiv \mathbf{p}_i$.

In the next sections, we introduce two different approximations based on the above space-time discretization. The former has been recently proposed in the literature in the simpler case of space-time data observed over planar domains [2] and represents the reference context for the numerical assessment of this paper; the latter coincides with the new proposed approach which aims at being computationally highly more effective.

3.1 A monolithic approach

We provide here the space-time discretization scheme proposed in [2]. The authors employ finite elements of degree r to approximate the space, combined with the θ-method for the time discretization. This leads to discretize time derivatives through an incremental ratio, whereas the other time-dependent terms are replaced by a convex linear combination of their values at times t_k and t_{k+1} [29]. In particular, in [2] the authors resort to the backward Euler scheme ($\theta = 1$), so that, for each $k = 1, \ldots, m-1$, the following system is solved

for $\hat{f}_h^{k+1}, g_h^k \in V_h^r(\mathcal{M})$

$$\begin{cases} \displaystyle\int_{\mathcal{M}} \rho_h \, g_h^k \, d\mathbf{p} + \int_{\mathcal{M}} \nabla_{\mathcal{M}} \hat{f}_h^{k+1} \cdot \nabla_{\mathcal{M}} \rho_h \, d\mathbf{p} + \int_{\mathcal{M}} \frac{\hat{f}_h^{k+1} - \hat{f}_h^k}{\Delta t} \rho_h \, d\mathbf{p} = 0 \\ \boldsymbol{\varphi}_n^T \hat{\mathbf{f}}_n^{k+1} + \lambda \displaystyle\int_{\mathcal{M}} \frac{g_h^{k+1} - g_h^k}{\Delta t} \varphi_h \, d\mathbf{p} \, - \lambda \int_{\mathcal{M}} \nabla_{\mathcal{M}} g_h^k \cdot \nabla_{\mathcal{M}} \varphi_h \, d\mathbf{p} = \boldsymbol{\varphi}_n^T \mathbf{z}_n^{k+1} \\ \hat{f}_h^1 = \tilde{f}_{h,1}, \quad g_h^m = \tilde{g}_{h,m}, \end{cases} \tag{8}$$

with $\rho_h, \varphi_h \in V_h^r(\mathcal{M})$, where $\hat{f}_h^j = \hat{f}_h(\mathbf{p}, t_j)$, $g_h^j = g_h(\mathbf{p}, t_j) \in V_h^r(\mathcal{M})$ denote the finite element approximation for function $\hat{f}$ and g, respectively at time t_j, with $j = 1, \ldots, m$, $\tilde{f}_{h,1}$ and $\tilde{g}_{h,m}$ are suitable approximations in $V_h^r(\mathcal{M})$ of the initial data $\tilde{f}_1$ and of the ending data $\tilde{g}_m$, where we have introduced the vectors $\hat{\mathbf{f}}_n^{k+1} = [\hat{f}_h(\mathbf{p}_1, t_{k+1}), \ldots, \hat{f}_h(\mathbf{p}_n, t_{k+1})]^T$, $\mathbf{z}_n^{k+1} = [z_{1k+1}, \ldots, z_{nk+1}]^T$, $\boldsymbol{\varphi}_n = [\varphi_h(\mathbf{p}_1), \ldots, \varphi_h(\mathbf{p}_n)]^T \in \mathbb{R}^n$. Notice that, according to this space-time approximation, the test functions are only space-dependent, in contrast to formulation (6) (and to the discretization adopted in the next section).
Following [15, 2], in order to provide the algebraic counterpart of system (8), we introduce the matrices of dimensionality $N_{\mathcal{T}}$

$$R_0 = \int_{\mathcal{M}} \boldsymbol{\psi} \boldsymbol{\psi}^T \, d\mathbf{p}, \qquad R_1 = \int_{\mathcal{M}} \nabla_{\mathcal{M}} \boldsymbol{\psi}^T \, (\nabla_{\mathcal{M}} \boldsymbol{\psi})^T \, d\mathbf{p},$$

where $(\nabla_{\mathcal{M}} \boldsymbol{\psi})^T$ is the transpose of the array $\nabla_{\mathcal{M}} \boldsymbol{\psi}(\mathbf{p}) = [\nabla \psi_1(\mathbf{p}), \ldots, \nabla \psi_{N_{\mathcal{T}}}(\mathbf{p})]^T$ collecting the gradient of the $N_{\mathcal{T}}$ finite element basis functions at the generic point $\mathbf{p} \in \mathcal{M}$, whereas $\nabla_{\mathcal{M}} \boldsymbol{\psi}^T = \nabla_{\mathcal{M}} \boldsymbol{\psi}^T(\mathbf{p}) = [(\nabla \psi_1)^T(\mathbf{p}), \ldots, (\nabla \psi_{N_{\mathcal{T}}})^T(\mathbf{p})]^T$. It follows that, for any $u_h, w_h \in V_h^r(\mathcal{M})$,

$$\int_{\mathcal{M}} u_h w_h \, d\mathbf{p} = \mathbf{u}^T R_0 \mathbf{w}, \qquad \int_{\mathcal{M}} \nabla_{\mathcal{M}} u_h \cdot \nabla_{\mathcal{M}} w_h \, d\mathbf{p} = \mathbf{u}^T R_1 \mathbf{w},$$

vectors $\mathbf{u} = [u_h(\boldsymbol{\xi}_1), \ldots, u_h(\boldsymbol{\xi}_{N_{\mathcal{T}}})]^T$, $\mathbf{w} = [w_h(\boldsymbol{\xi}_1), \ldots, w_h(\boldsymbol{\xi}_{N_{\mathcal{T}}})]^T \in \mathbb{R}^{N_{\mathcal{T}}}$ gathering the values taken by functions u_h and w_h at the mesh nodes.
From now on, we take $r = 1$, so that $N_{\mathcal{T}} = n$. Thus, the algebraic counterpart of the space-time discretization in (8) turns out to be

$$\begin{cases} R_0 \mathbf{g}_n^k + R_1 \hat{\mathbf{f}}_n^{k+1} + R_0 \dfrac{\hat{\mathbf{f}}_n^{k+1} - \hat{\mathbf{f}}_n^k}{\Delta t} = 0 \\ \Psi^T \Psi \hat{\mathbf{f}}_n^{k+1} + \lambda R_0 \dfrac{\mathbf{g}_n^{k+1} - \mathbf{g}_n^k}{\Delta t} - \lambda R_1 \mathbf{g}_n^k = \Psi^T \mathbf{z}_n^{k+1}, \end{cases} \tag{9}$$

with $k = 1, \ldots, m-1$, $\hat{\mathbf{f}}_n^1 = [\tilde{f}_{h,1}(\mathbf{p}_1), \ldots, \tilde{f}_{h,1}(\mathbf{p}_n)]^T$, $\mathbf{g}_n^m = [\tilde{g}_{h,m}(\mathbf{p}_1), \ldots, \tilde{g}_{h,m}(\mathbf{p}_n)]^T \in \mathbb{R}^n$, and where, in accordance with the notation in (7), $\hat{\mathbf{f}}_n^k = [\hat{f}_h(\mathbf{p}_1, t_k), \ldots, \hat{f}_h(\mathbf{p}_n, t_k)]^T$, $\mathbf{g}_n^j = [g_h(\mathbf{p}_1, t_j), \ldots, g_h(\mathbf{p}_n, t_j)]^T \in \mathbb{R}^n$ for $j = k, k+1$.

System (9) is sparse since the Lagrangian basis $\mathcal{B}$ is locally supported. Nevertheless, the system is fully coupled due to the opposite time direction characterizing the equations

for $\hat{f}_h$ and g_h. Such a coupling leads to adopt a monolithic approach when solving (9), which considers all the involved times, simultaneously [2]. This approach might represent an issue from a computational viewpoint, in particular when dealing with large datasets (i.e., for large values of m and n). Indeed, the dimensionality of system (9) turns out to be equal to $2mn$. As a consequence, complex geometries or long time-series are ruled out by the monolithic method, which, in such contexts, becomes very time- and memory-consuming. This is the case of the applications tackled in Section 5 which are out of reach for the monolithic approach when codes are run on a standard laptop[1].
These restrictions justify the proposal in the next section of a new procedure, which offers us an alternative to the monolithic approach.

3.2 A new fixed point-based algorithm

The procedure here proposed aims at commuting the whole system (9) into m smaller problems in order to make affordable the management of complex amounts of data.
To tackle the coupling between the two equations in (9), we resort to a fixed point approach [29]. Additionally, we adopt a space-time discretization alternative to the one characterizing the monolithic approach. In particular, to be compliant with the weak formulation in (6), where the trial and the test functions depend both on the space and time, we employ space-time finite elements, continuous in space and time [33, 12]. Thus, in the generic time interval, $(\tau_{k-1}, \tau_k]$, a fully discrete function, w_h, can be expanded as $\sum_{j=0}^{s} t^j w_{h,j}(\mathbf{p})$, i.e., as a linear combination of functions, $w_{h,j}$, belonging to the finite element space, $V_h^r(\mathcal{M})$, with coefficients coinciding with suitable powers of the time independent variable, t. Throughout the paper, we make the choice $r = 1$, $s = 0$ in view of a fair comparison between the monolithic and the new approach.
We replace the algebraic system (9) with the new one

$$\begin{cases} R_0 \mathbf{g}_n^{k+1} + R_1 \hat{\mathbf{f}}_n^{k+1} + R_0 \dfrac{\hat{\mathbf{f}}_n^{k+1} - \hat{\mathbf{f}}_n^{k}}{\Delta t} = 0 \\ \Psi^T \Psi \hat{\mathbf{f}}_n^{k} + \lambda R_0 \dfrac{\mathbf{g}_n^{k+1} - \mathbf{g}_n^{k}}{\Delta t} - \lambda R_1 \mathbf{g}_n^{k} = \Psi^T \mathbf{z}_n^{k}, \end{cases} \tag{10}$$

with $k = 1, \ldots, m-1$, $\hat{\mathbf{f}}_n^1 = [\tilde{f}_{h,1}(\mathbf{p}_1), \ldots, \tilde{f}_{h,1}(\mathbf{p}_n)]^T$, $\mathbf{g}_n^m = [\tilde{g}_{h,m}(\mathbf{p}_1), \ldots, \tilde{g}_{h,m}(\mathbf{p}_n)]^T \in \mathbb{R}^n$, and where the same notations as in (9) are here adopted. Analogously to a semi-implicit scheme, all the time-dependent terms in the equation associated with $\hat{f}$ are evaluated at time t^{k+1}, whereas the time-dependent contributions in the equation to be solved for g are considered at time t^k.

Now, for each $k = 1, \ldots, m$, we yield a sequence of approximations $\{(\hat{\mathbf{f}}_n^{k,j}, \mathbf{g}_n^{k,j})\}$ for the solution $(\hat{\mathbf{f}}_n^k, \mathbf{g}_n^k)$ of system (10) via an iterative fixed point algorithm, j being the fixed point iteration index. Then, a check on the accuracy, combined with a maximum number of iterations, is used to stop the iterative procedure.
To start the algorithm, we have to select the initial guess. In particular:

[1]The computations of the paper have been run on a Asus Intel Core i7-7700HQ 2.80GHZ 16GB desktop computer.

1. we compute the values $\hat{\mathbf{f}}_n^{k,0}$, for $k = 2, \ldots, m$, by referring to the steady case (see Proposition 2 in [15]), i.e., by solving the $(m-1)$ problems

$$(\Psi^T\Psi + \lambda R_1 R_0^{-1} R_1)\,\hat{\mathbf{f}}_n^{k,0} = \Psi^T \mathbf{z}_n^k; \tag{11}$$

2. we compute the values $\mathbf{g}_n^{k,0}$, for $k = m-1, \ldots, 1$, by solving the $(m-1)$ problems

$$\Psi^T\Psi\,\hat{\mathbf{f}}_n^{k,0} + \lambda R_0 \frac{\mathbf{g}_n^{k+1,0} - \mathbf{g}_n^{k,0}}{\Delta t} - \lambda R_1 \mathbf{g}_n^{k,0} = \Psi^T \mathbf{z}_n^k \tag{12}$$

by using the values obtained in (11) for the vectors $\hat{\mathbf{f}}_n^{k,0}$, for $k = 2, \ldots, m$, and by setting, for simplicity, $\mathbf{g}_n^{m,0} = \mathbf{0}$ and $\hat{\mathbf{f}}_n^{1,0} = \hat{\mathbf{f}}_n^1$.

Then, at the generic iteration, j (with $j \geq 1$), of the fixed point scheme, we update the pair $(\hat{\mathbf{f}}_n^{k,j-1}, \mathbf{g}_n^{k,j-1})$, for $k = 1, \ldots, m$, by computing the new pair $(\hat{\mathbf{f}}_n^{k,j}, \mathbf{g}_n^{k,j})$, such that:

i) for $k = 1$,

$$\begin{cases} \hat{\mathbf{f}}_n^{1,j} = \hat{\mathbf{f}}_n^1 \\ \lambda\Big(R_1 + \dfrac{1}{\Delta t} R_0\Big)\mathbf{g}_n^{1,j} = \dfrac{\lambda}{\Delta t} R_0 \mathbf{g}_n^{2,j-1} + \Psi^T(\Psi\hat{\mathbf{f}}_n^1 - \mathbf{z}_n^1); \end{cases}$$

ii) for $k = 2, \ldots, m-1$,

$$\begin{bmatrix} R_1 + \dfrac{1}{\Delta t} R_0 & R_0 \\ \Psi^T\Psi & -\lambda\Big(R_1 + \dfrac{1}{\Delta t} R_0\Big) \end{bmatrix} \begin{bmatrix} \hat{\mathbf{f}}_n^{k,j} \\ \mathbf{g}_n^{k,j} \end{bmatrix} = \begin{bmatrix} \dfrac{1}{\Delta t} R_0 \hat{\mathbf{f}}_n^{k-1,j-1} \\ \Psi^T \mathbf{z}_n^k - \dfrac{\lambda}{\Delta t} R_0 \mathbf{g}_n^{k+1,j-1} \end{bmatrix};$$

iii) for $k = m$,

$$\begin{cases} \Big(R_1 + \dfrac{1}{\Delta t} R_0\Big)\hat{\mathbf{f}}_n^{m,j} = \Big(\dfrac{1}{\Delta t} R_0 \hat{\mathbf{f}}_n^{m-1,j-1} - R_0 \mathbf{g}_n^{m,j-1}\Big) \\ \mathbf{g}_n^{m,j} = \mathbf{0}. \end{cases}$$

The decoupling effect introduced by the fixed point iterations allows us to carry out all the computations in i)-iii) simultaneously, in the spirit of a Jacobi solver.
The algorithm is stopped by introducing a tolerance, `TOL`, on the relative variation of the cost functional J_λ in (2), when evaluated on two consecutive approximations, and after setting a maximum number, `NMax`, of iterations.

The two next sections are meant to numerically investigate the reliability and the efficiency of the fixed point-based algorithm, first when applied to simulation case studies and then by considering a real datasets.

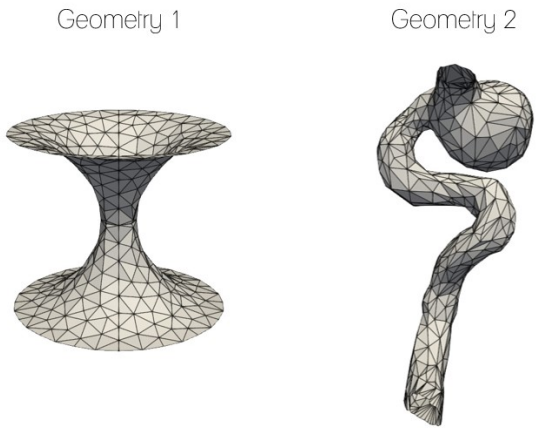

Figure 2: Geometries for the simulation studies. Geometry 1: a benchmark geometry. Geometry 2: simplification of a patient-specific inner carotid artery affected by an aneurysm.

4 Simulation studies

In this section we assess the performances of the new algorithm introduced in Section 3.2 when applied to spatio-temporal data. We compare the proposed method with kriging, the most commonly used technique to analyze spatial and spatio-temporal data (see, e.g., [8] and the references therein). Kriging does not work on generic manifolds. For this reason, to perform the comparison with the new fixed point-based procedure, we combine kriging with a conformal flattening map approach, as detailed below.

Figure 2 shows the two test domains we considered for comparison purposes. The first domain is a benchmark geometry, employed, for instance, in [15], here discretized by a mesh with 340 vertices. The second domain coincides with the geometry of a vessel, obtained after simplifying the patient-specific morphology of an inner carotid artery affected by an aneurysm, shown in the left panel of Figure 8 [1]. This geometry is of relevance for the investigation carried out in Section 5.1. The mesh in the right panel of Figure 2, which discretizes the vessel geometry, is characterized by 600 vertices.
To generate data, over each manifold we consider 50 smooth functions defined by

$$f(\mathbf{p},t) = a_1 \cos\left(2\pi\, p_{[1]}\left(1+\frac{t}{0.2}\right)\right) + a_2 \cos\left(2\pi\, p_{[2]}\,\frac{t}{0.2}\right) + a_3 \cos(2\pi\, p_{[3]}) \cos\left(2\pi\,\frac{t}{0.2}\right), \tag{13}$$

with $\mathbf{p} = [p_{[1]}, p_{[2]}, p_{[3]}]^T$, and where the coefficients a_j, for $j = 1, 2, 3$, are randomly generated from independent normal distributions, with mean equal to 0 and standard deviation equal to 1. Then, these functions are evaluated at the mesh vertices (so that the data locations, $\mathbf{p}_1, \ldots, \mathbf{p}_n$, coincide with mesh vertices/nodes), in correspondence with 31 equispaced times in the time window $[0, 0.3]$. The collected values are hence corrupted by an additive independent Gaussian noise, with mean equal to 0 and variance equal to 0.5. The noise level ranges approximately from 0% to 60% of the true signal.

The first column in Figures 3 and 4 shows the first smooth function generated according to (13) at different times, over Geometry 1 and 2, respectively. The second column in the same figures provides the corresponding sampled noisy data, at the same times.

Now, starting from the noisy data, we resort to the fixed-point based algorithm proposed in Section 3.2 to estimate the fifty smooth functions generated over the two benchmark geometries. To this aim, for both the test domains and for each simulation repetition, we select the smoothing parameter λ in (2) via 5-fold cross validation [19], while constraining the fixed-point iterations with parameters `TOL`$=$ 5e-04 and `NMax`$=$ 30. The fixed point algorithm converges, on average, after 5 and 6 iterations for Geometry 1 and 2, respectively. The third columns in Figures 3 and 4 show the corresponding estimation, at the different times. The matching with the original data is very good, despite the noise characterizing the sampled data.

For the sake of comparison, we compute now the estimates by kriging.
The bi-dimensional spatial domains kriging is able to handle are planar or spherical. This is not the case of Geometries 1 and 2. As a consequence, to implement kriging, we resort to a conformal flattening procedure according to what described in [18]. In more detail, following [15], we introduce a continuously differentiable map which changes the Riemannian manifold $\mathcal{M} \subset \mathbb{R}^3$ into a planar domain $\Omega \subset \mathbb{R}^2$. As an example, Figure 5 shows the result of the conformal flattening when applied to Geometry 1. Note that kriging does not employ the flattened mesh. This simply provides the location of the data on the conformally flattened domain, the data being located at the vertices of the planar mesh. Kriging is thus implemented over the flattened Geometries 1 and 2, by using the R package *gStat* [25]. In particular, we consider a separable variogram, marginally exponential in space and Gaussian in time, whose parameters, for each simulation replicate, are estimated starting from the values of the empirical variogram, as it is a standard practice for kriging.
Moreover, spatio-temporal kriging cannot handle too large datasets. This justifies the simplification we have applied to the original geometry of the patient-specific inner carotid artery (with an associated original mesh of 6017 vertices) to yield the mesh in Figure 2, right panel, consisting of 600 vertices only. The mesh simplification has been performed by exploiting the algorithm in [10]. The fourth columns in Figures 3 and 4 provide the spatio-temporal kriging estimates at the considered times. A qualitative cross comparison among the third and the fourth columns in the two figures highlights the superior performances of the new algorithm proposed in Section 3.2.

We enrich the comparative analysis between the fixed point-based procedure and kriging by including the monolithic method adopted in [2] and summarized in Section 3.1. The monolithic approach yields estimates which, from a qualitative viewpoint, are fully comparable with the results provided by the fixed point-based algorithm. Nevertheless, a quantitative investigation highlights that the method proposed in this paper outperforms the monolithic formulation in terms of computational efficiency. The quantitative analysis is carried out by computing, for each test domain and for each simulation repetition, the

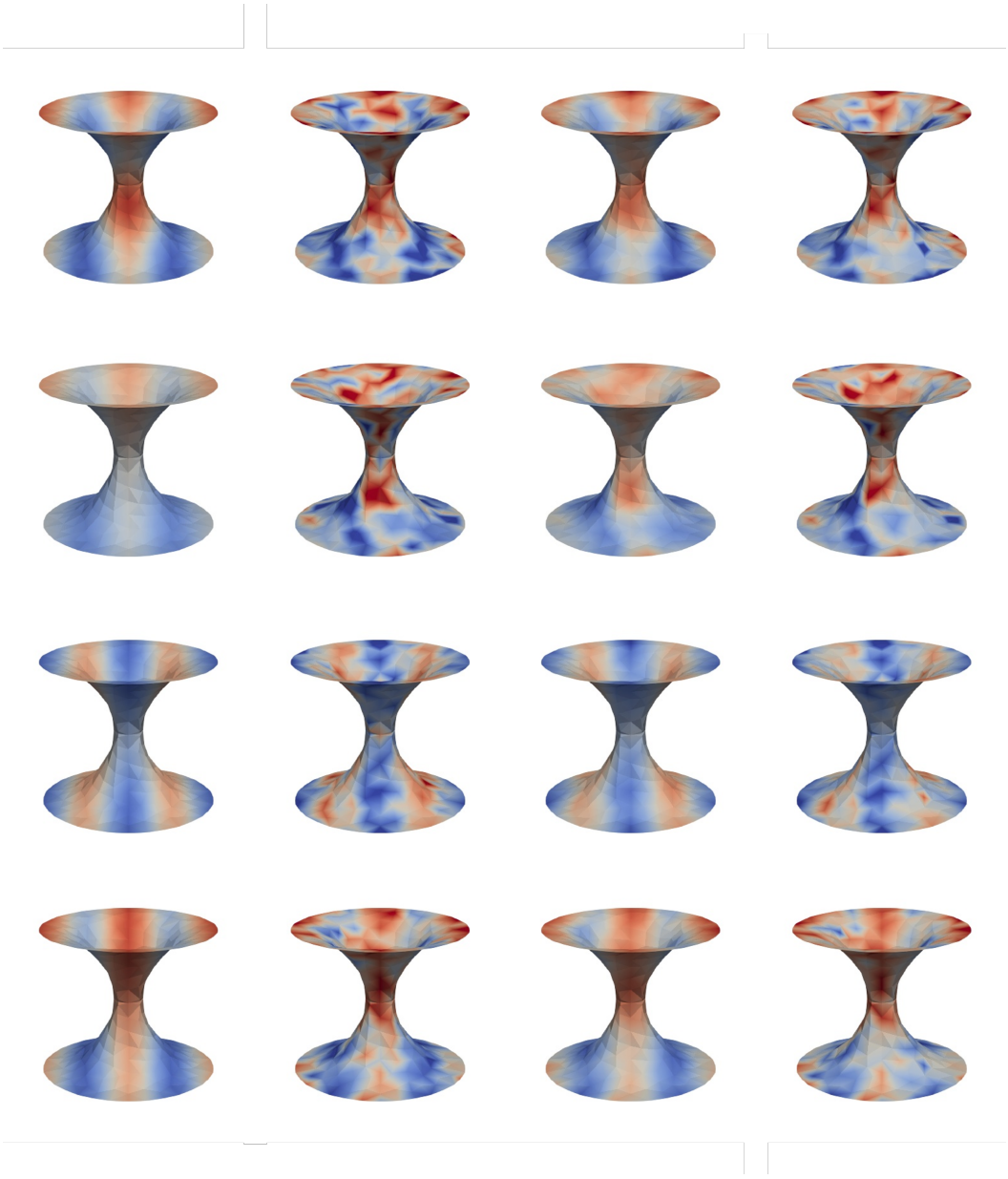

Figure 3: Geometry 1: true function f (first column) generated in the first simulation repetition, at time $t = 0$[s] (first row), 0.05[s] (second row), 0.1[s] (third row) and 0.15[s] (last row); noisy data (second column); estimate provided by the proposed fixed point-based algorithm (third column) and by the spatio-temporal kriging (fourth colum).

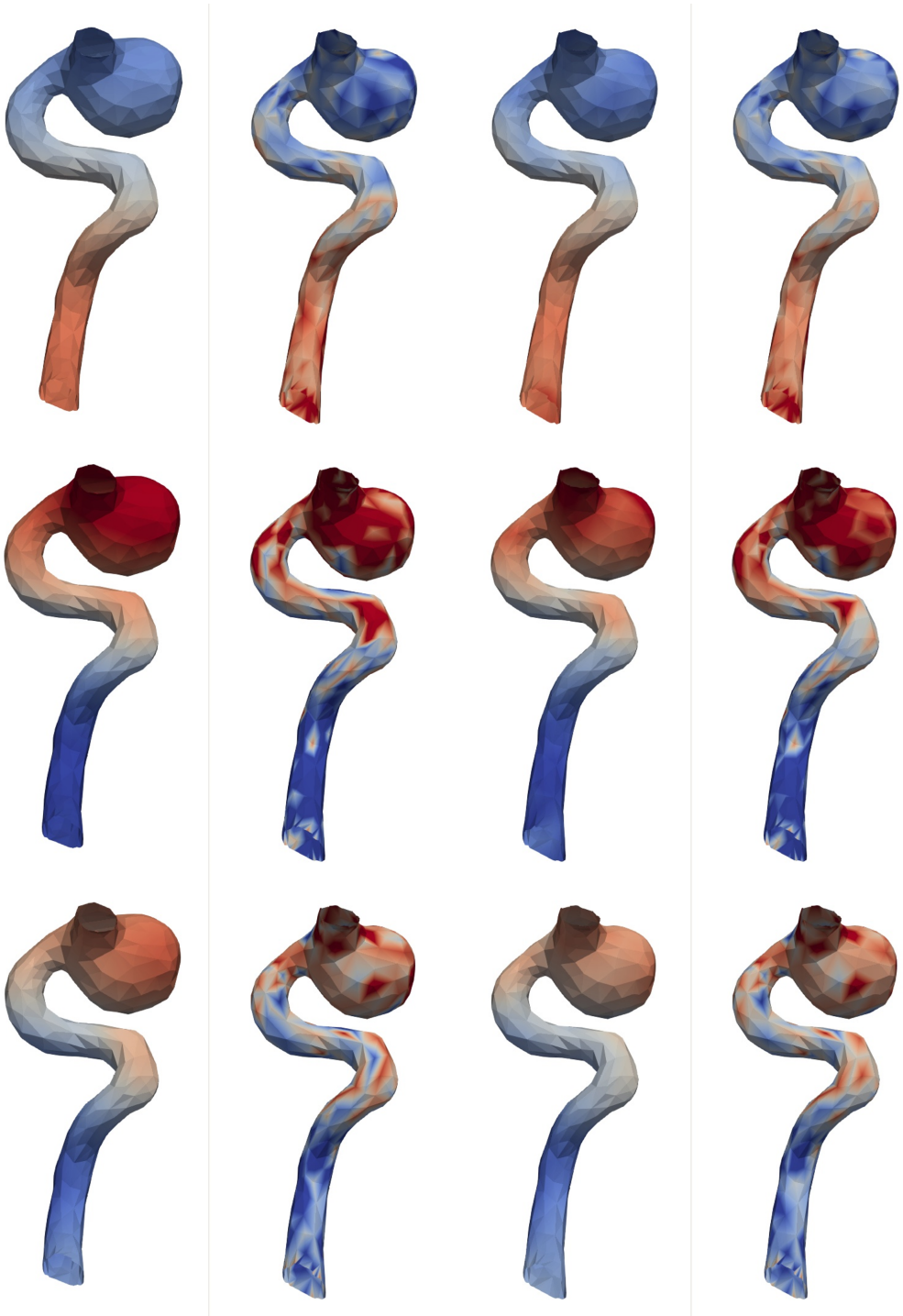

Figure 4: Geometry 2: true function f (first column) generated in the first simulation repetition, at time $t = 0$[s] (first row), 0.05[s] (second row), 0.1[s] (third row); noisy data (second column); estimate provided by the proposed fixed point-based algorithm (third column) and by the spatio-temporal kriging (fourth colum).

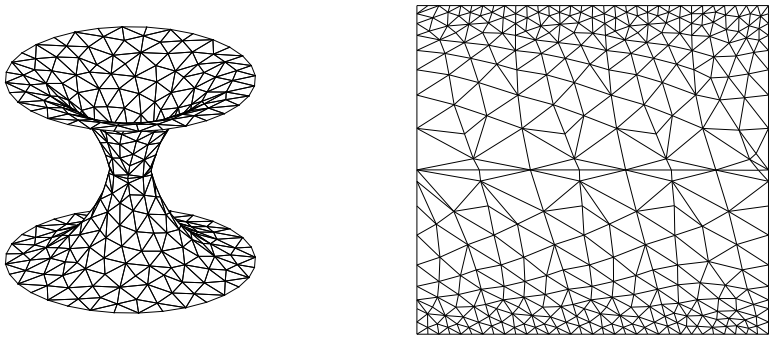

Figure 5: Geometry 1: original geometry (left); conformal flattening of the geometry used for the implementation of kriging (right).

Mean Square Error,

$$\mathrm{MSE} = \frac{\sum_{i=1}^{n}\sum_{j=1}^{m}\left[f(\mathbf{p}_i, t_j) - \hat{f}(\mathbf{p}_i, t_j)\right]^2}{nm},$$

associated with the corresponding estimate, $\hat{f}$, and the CPU time required by the computational procedure. Figure 6 collects the box plots for the MSE characterizing the three methods here compared, and for both the geometries. The performance of the fixed point-based algorithm and of the monolithic approach in terms of MSE is essentially the same. Instead, kriging is characterized by a significantly higher MSE, with a large dispersion and several outliers associated with very high MSE values. As expected, the estimates yielded by the new and by the monolithic algorithms turn out to be more robust, as highlighted by the contained dispersion of the associated MSEs.
Figure 7 displays the box plots for the execution time, measured in seconds ([s]), demanded by the fixed point-based and by the monolithic methods, when run on the two test geometries. This check reveals the evident superiority of the new algorithm with respect to the monolithic approach in terms of numerical efficiency, with a reduction of the execution time, on average, of about 5 times for both the geometries. Kriging has not been included in the figure, due to the remarkably higher time characterizing such a method (around 4 minutes for both the geometries instead of few seconds).

5 Case studies

We here illustrate the effectiveness of the fixed point-based method through two applied case studies, after having verified the reliability and the computational efficiency of such an approach in the previous section.
The first case study concerns the analysis of the shear-stress exerted by the blood-flow over

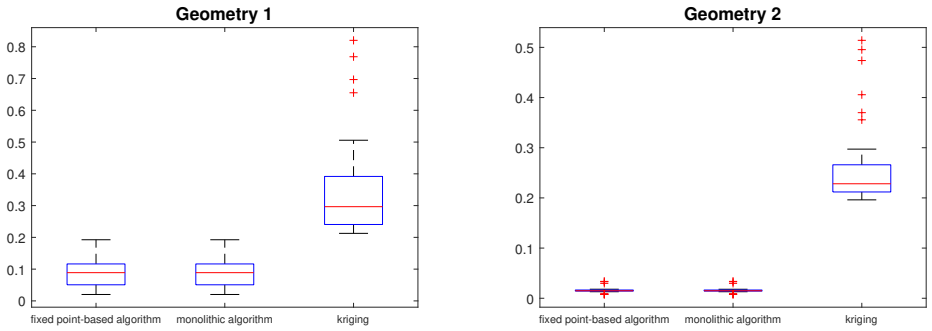

Figure 6: Geometries 1 and 2: box plots for the Mean Square Error (MSE) associated with the estimates provided by the fixed point-based method, by the monolithic approach and by kriging, over the 50 simulation repetitions with test functions generated as in (13).

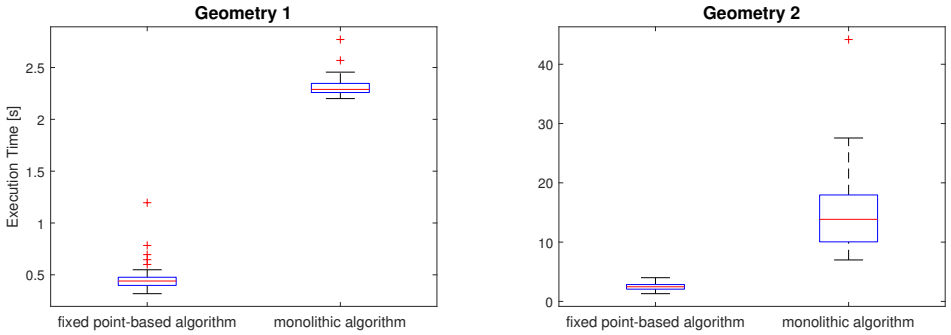

Figure 7: Geometries 1 and 2: box plots for the execution time ([s]) associated with the estimates provided by the fixed point-based and by the monolithic approach over the 50 simulation repetitions with test functions generated as in (13).

the wall of an inner carotid artery. The second application comes from the neurosciences and deals with the study of the neuronal activity on the cerebral cortex. Standard kriging cannot be used in these real-word applications (not even disregarding the complex geometry of the domains), due to the high dimensionality of the data.

5.1 Study of heamodynamic forces on the arterial walls

As a first practical case study, we consider a medical disease whose incidence in the population is very high (around 10 cases per 100000 people, with mortality or serious health conditions in 60% of cases [30]). We are referring to the rupture of a cerebral aneurysm, namely, of a large bulge that may modify the standard shape of a vessel wall in the brain. These deformations are very common in the adult population. In the vast majority of cases, cerebral aneurysms are totally asymptomatic and innocuous. The rupture of an aneurysm is an infrequent event, but unfortunately characterized by a very high mortality.
The origin of this pathology is still largely unknown. The study of the factors causing the

development and the possible rupture of aneurysms has attracted lot of interest in the scientific and medical community (see, e.g., [24, 3]). It is believed that one of the main features influencing the aneurysm pathogenesis is the shear-stress exerted by the blood flow on the arterial wall. In particular, a strong variation of the shear-stress in space, and over the time of the heart-beat, is conjectured to be associated with the aneurysms formation, development and possible rupture; moreover, very low values of shear-stress are thought to be very dangerous (see [3] and references therein). This haemodynamic stress is in turn dependent on the complex morphology of the vessel. For this reason, the study of the spatio-temporal behavior of the shear-stress in patient-specific geometries of arteries affected by cerebral aneurysms, is of great interest for advancing the knowledge on this pathology.

Figure 8 shows the considered medical configuration. It coincides with a patient-specific inner carotid artery affected by a large aneurysm. In particular, the wall of the artery has been discretized by a triangular mesh consisting of 6017 vertices (see Figure 8, left). Actually, we are dealing with the same manifold as in Section 4 (Geometry 2). However, the computational efficiency of the fixed point-based algorithm allows us to involve here a finer discretization of such a geometry, with a consequent higher reliability of the associated analysis. Concerning the analyzed data, we refer to the AneuRisk project [1]. In particular, we consider the modulus of the wall shear-stress obtained from computational fluid dynamics simulations [23, 26]. This quantity is available at the mesh vertices, at 100 temporal instants, that cover a full heart-beat. A first analysis of these data has been carried out in [15], although restricted to a single time-instant.

Now, we exploit the fixed point-based approach to estimate the spatial wall shear-stress distribution over the inner carotid artery at two distinct times during the heart beat. For this purpose, we choose the smoothing parameter λ by 5-fold cross validation, while selecting values 1e-04 and 50 for parameters `TOL` and `NMax`, respectively. Six fixed point iterations are demanded, on average, to ensure the convergence at each time, leading to a total elapsed time equal to 16.28 seconds. Figure 8 compares the raw (middle panels) with the estimated (right panels) wall shear-stress. A visual inspection does not highlight differences between the observed and the smoothed data. This is due to the fact that these data, obtained by computational fluid dynamics simulations, are characterized by very low noise, i.e., order of magnitude lower than the data values. For this reason, the proposed algorithm, that correctly identifies the very high signal-to-noise ratio in the data, only filters out the high-frequency variation in the observations. Of course, a higher value of the smoothing parameter λ could be used to return a smoother estimate, that highlights only the main patterns of the signal. The displayed temporal instants are characterized by a significative variation in the shear-stress distribution, in particular with low values of the shear stress within the aneurysmal sac. Independently of the selected time instants, it can be checked that in this location the wall shear-stress remains always very low and fluctuating, thus supporting the conjecture that low values of this stress play a major role in the aneurysmal pathogenesis.

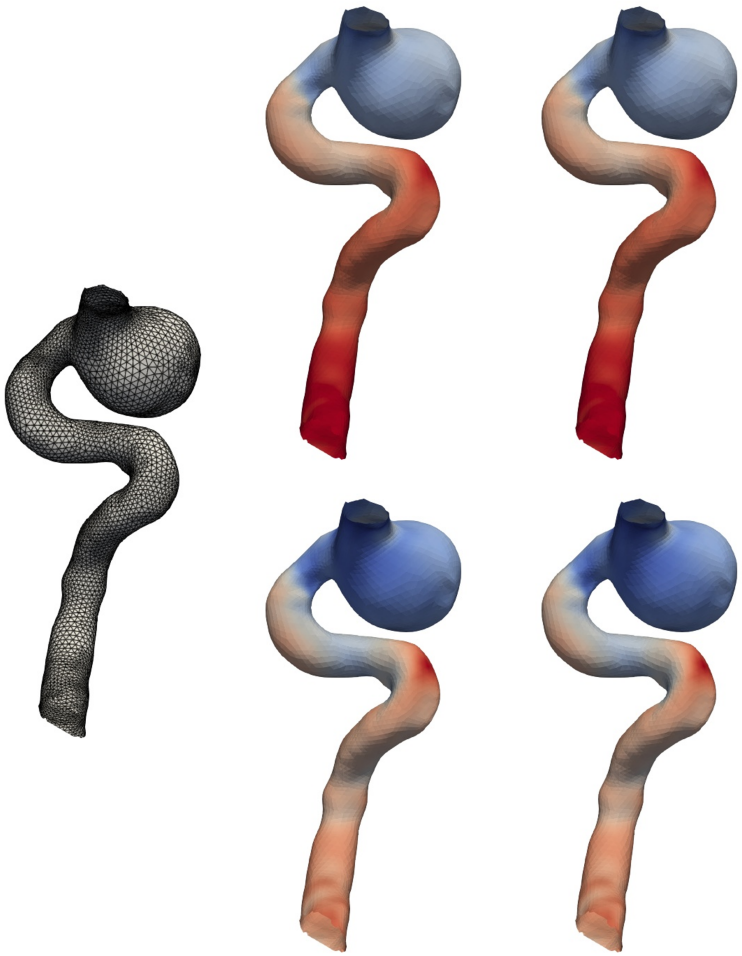

Figure 8: Heamodynamic case study: discretization of the inner carotid artery (left); observed wall shear-stress (middle) and corresponding estimate provided by the fixed point-based approach (right) at two different temporal instants (top-bottom) during the heart beat.

5.2 Study of neuronal activity on the cerebral cortex

The cerebral cortex is the outermost part of the brain - a thin layer of neural tissue where most of the neuronal activity takes place. From a geometric viewpoint, the cerebral cortex coincides with a highly tangled surface. It can be approximated by a triangular mesh which, unavoidably, turns out to be very complex, as shown in left panel of Figure 1. On the top of this two-dimensional manifold domain, it can be observed a time-varying hemodynamic signal associated with the neuronal activity on the cerebral cortex. Figure 1 shows one temporal snapshot of such a hemodynamic signal, measured during a functional Magnetic Resonance Imaging (fMRI) scan. The propagation of this signal constitutes the object of our investigation.

The data here analyzed come from the Human Connectome Project, a wide public database of resting-state and task-based fMRI scans, structural scans, diffusion MRI scans, from a large number of volunteers [14]. Currently, there is a strong effort in the scientific community in setting up methods for the analysis of this kind of data (see, e.g., [6, 9, 36]), with the common goal of advancing the knowledge on cerebral functioning and diseases. Despite this considerable interest, the most part of neuroimaging studies is still carried out either by disregarding the spatial dependence in the signal, or by employing basic methods which exploit the standard Euclidean distance. These simplified endeavours may lead to inaccurate estimates, for instance since functional distinct areas, that are apart over the cortex, result close in three-dimensional space due to the presence of a sulcus. Actually, it has been proved that the possibility to include the highly complex brain anatomy in the data analysis turns out to be a necessary step in order to guarantee a reliable investigation [16, 22]. The method adopted in this paper offers a spatio-temporal smoothing procedure able to correctly comply with the cerebral cortex morphology.

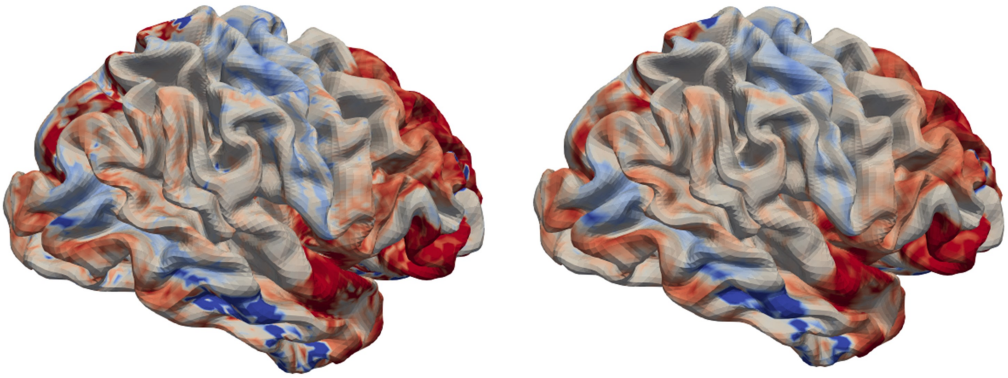

Figure 9: Neuroimaging case study: observed signal at a fixed temporal instant (left) and corresponding estimate provided by the fixed point-based approach (right).

To assess the fixed point-based algorithm, we start from the data associated with the

triangular mesh in the left panel of Figure 1, consisting of 32492 vertices. The data coincide with the fMRI signals induced over a patient-specific cerebral cortex by the neuronal activity, at 30 temporal instants. The left panel in Figure 9 shows a specific temporal snapshot of this signal. Starting from these noisy data, we run the algorithm proposed in Section 3.2 to estimate the underlying smooth spatio-temporal signal on the cerebral cortex. To this aim, we select the smoothing parameter in (2) by 5-fold cross validation and we set the two parameters, `NMax` and `TOL`, characterizing the stopping check to 50 and 1e-04, respectively. The fixed point algorithm converges, on average, within 15 iterations, while the whole estimation process takes 400.16 seconds. Figure 9, compares the raw data (left panel) with the smooth estimate provided by fixed point algorithm (right panel), at the considered temporal instant. A visual comparison between the two panels highlights the accuracy of the estimate, that is able to efficiently smooth the data, appropriately filtering out the noise without generating any artifact. In particular, notice that the data values observed over nearby gyri are not artificially linked by the algorithm.
Finally, we remark that higher values for parameter λ could also be used in order to yield an estimate that only captures the macroscopic features of the original signal, thus returning the corresponding main pattern.

6 Discussion and possible enhancements

The proposed fixed point-based approach turns out to be an ideal tool to analyze large amount of spatio-temporal data over general manifolds in $\mathbb{R}^3$. The numerical assessment in Section 4 shows the superiority of such a new method when compared both with kriging (combined with a conformal flattening of the domain to manage generic manifolds) and with the monolithic procedure proposed in [2], here adapted to non-planar domains. In particular, the fixed point-based algorithm is considerably more reliable than kriging (Figures 3, 4, 6). On the other hand, when compared with the monolithic approach, the new method reveals to be significantly more efficient in terms of computational time (Figure 7) without waiving the estimate accuracy (Figure 6), and allows us to handle data over general two-dimensional Riemannian manifolds. The gained effectiveness guarantees the possibility to estimate massive datasets as corroborated by the applicative settings analyzed in Section 5.

The method introduced in this paper enables several extensions. Among the most interesting ones, we cite the inclusion of space-varying covariates in a semi-parametric setting, analogously to what discussed in [32, 15] for the simplified case of spatial data only. In the heamodynamic framework, this feature would allow us to include into the estimation process the space-varying radius and the curvature of the vessel, to study the role played by these geometrical features in cerebral aneurysm pathology. In the application to neuroimaging data, we would take into account the space-varying cortical thickness, which may have an effect on the hemodynamic signal here considered.
Another interesting generalization concerns the adopted finite element discretization which could be replaced by an isogeometric analysis, thus generalizing what done in [35] in a steady setting.

Acknowledgments. We are grateful to Eardi Lila for helping us in the processing of the brain imaging data. We also thank Bree Ettinger, who provided us the code implementing the conformal flattening used in Section 4, for comparison purposes with kriging. Finally, the second author acknowledges the research project GNCS-INdAM 2020 "Tecniche Numeriche Avanzate per Applicazioni Industriali".

References

[1] Aneurisk project. https://statistics.mox.polimi.it/aneurisk/.

[2] Eleonora Arnone, Laura Azzimonti, Fabio Nobile, and Laura M. Sangalli. Modeling spatially dependent functional data via regression with differential regularization. *J. Multivariate Anal.*, 170:275–295, 2019.

[3] S. Bacigaluppi, M. Piccinelli, L. Antiga, A. Veneziani, T. Passerini, P. Rampini, M. Zavanone, P. Severi, G. Tredici, G. Zona, T. Krings, E. Boccardi, S. Penco, and M. Fontanella. Factors affecting formation and rupture of intracranial saccular aneurysms. *Neurosurgical Review*, 37:1–14, 2014.

[4] V. Baramidze, M. J. Lai, and C. K. Shum. Spherical splines for data interpolation and fitting. *SIAM J. Sci. Comput.*, 28(1):241–259, 2006.

[5] Stefano Castruccio and Michael L. Stein. Global space-time models for climate ensembles. *Ann. Appl. Stat.*, 7(3):1593–1611, 2013.

[6] M.K. Chung, J.L. Hanson, and S.D Pollak. Statistical analysis on brain surfaces. In *Handbook of Modern Statistical Methods: Neuroimaging Data Analysis*, Chapman & Hall/CRC Handbooks of Modern Statistical Methods, pages 233–262. CRC Press, Boca Raton, FL, 2017.

[7] Moo K. Chung, Steven M. Robbins, Kim M. Dalton, Richard J. Davidson, Andrew L. Alexander, and Alan C. Evans. Cortical thickness analysis in autism with heat kernel smoothing. *NeuroImage*, 25:1256–1265, 2005.

[8] N. Cressie and C.K. Wikle. *Statistics for Spatio-Temporal Data*. Wiley, 2011.

[9] F. Dassi, J.M. Kroos, L. Gerardo-Giorda, and S. Perotto. A denoising tool for the reconstruction of cortical geometries from MRI. *Math. Comput. Simulation*, 191:14–32, 2022.

[10] Franco Dassi, Bree Ettinger, Simona Perotto, and Laura M. Sangalli. A mesh simplification strategy for a spatial regression analysis over the cortical surface of the brain. *Appl. Numer. Math.*, 90:111–131, 2015.

[11] Tom Duchamp and Werner Stuetzle. Spline smoothing on surfaces. *J. Comput. Graph. Statist.*, 12(2):354–381, 2003.

[12] K. Eriksson, D. Estep, P. Hansbo, and C. Johnson. *Computational differential equations*. Cambridge University Press, Cambridge, 1996.

[13] A. Ern and J.-L. Guermond. *Theory and Practice of Finite Elements*, volume 159 of *Applied Mathematical Sciences*. Springer-Verlag, New York, 2004.

[14] D.C. Van Essen, K. Ugurbil, E. Auerbach, D. Barch, T.E.J. Behrens, R. Bucholz, A. Chang, L. Chen, M. Corbetta, S.W. Curtiss, S. Della Penna, D. Feinberg, M.F. Glasser, N. Harel, A.C. Heath, L. Larson-Prior, D. Marcus, G. Michalareas, S. Moeller, R. Oostenveld, S.E. Petersen, F. Prior, B.L. Schlaggar, S.M. Smith, A.Z. Snyder, J. Xu, and E. Yacoub. The human connectome project: A data acquisition perspective. *NeuroImage*, 62(4):2222 – 2231, 2012.

[15] Bree Ettinger, Simona Perotto, and Laura M. Sangalli. Spatial regression models over two-dimensional manifolds. *Biometrika*, 103(1):71–88, 2016.

[16] Matthew F. Glasser, Stamatios N. Sotiropoulos, J. Anthony Wilson, Timothy S. Coalson, Bruce Fischl, Jesper L. Andersson, Junqian Xu, Saad Jbabdi, Matthew Webster, Jonathan R. Polimeni, David C. Van Essen, and Mark Jenkinson. The minimal preprocessing pipelines for the human connectome project. *NeuroImage*, 80(0):105 – 124, 2013.

[17] D. J. Hagler, Jr., A. P. Saygin, and M. I. Sereno. Smoothing and cluster thresholding for cortical surface-based group analysis of fMRI data. *NeuroImage*, 33:1093–1103, 2006.

[18] S. Halier, S. Angenent, A. Tannenbaurn, and R. Kikinis. Nondistorting flattening maps and the 3-d visualization of colon ct images. *IEEE Transactions on Medical Imaging*, 19(7):665–670, 2000.

[19] Trevor Hastie, Robert Tibshirani, and Jerome Friedman. *The elements of statistical learning*. Springer Series in Statistics. Springer, New York, second edition, 2009. Data mining, inference, and prediction.

[20] Jaehong Jeong and Mikyoung Jun. A class of Matérn-like covariance functions for smooth processes on a sphere. *Spat. Stat.*, 11:1–18, 2015.

[21] Ming-Jun Lai, C. K. Shum, V. Baramidze, and P. Wenston. Triangulated spherical splines for geopotential reconstruction. *J. Geodesy*, 83(4):695–708, 2009.

[22] Eardi Lila, John A. D. Aston, and Laura M. Sangalli. Smooth Principal Component Analysis over two-dimensional manifolds with an application to neuroimaging. *Ann. Appl. Stat.*, 10(4):1854–1879, 2016.

[23] Tiziano Passerini. *Computational hemodynamics of the cerebral circulation: multiscale modeling from the circle of willis to cerebral aneurysms*. PhD thesis, Politecnico di Milano, 2009.

[24] Tiziano Passerini, Laura M. Sangalli, Simone Vantini, Marina Piccinelli, Susanna Bacigaluppi, Luca Antiga, Edoardo Boccardi, Piercesare Secchi, and Alessandro Veneziani. Integrated statistical investigation of internal carotid arteries of patients affected by cerebral aneurysms. *Cardiovasc Eng Tech*, 3:26–40, 2012.

[25] E.J. Pebesma. Multivariable geostatistics in s: the gstat package. *Computers & Geosciences*, 30:683–691, 2004.

[26] Marina Piccinelli, Alessandro Veneziani, D.A. Steimann, A. Remuzzi, and Luca Antiga. A framework for geometric analysis of 852 vascular structures: Applications to cerebral aneurysms. *IEEE Trans. Med. Imag.*, 28:1141–1155, 2009.

[27] Emilio Porcu, Alfredo Alegria, and Reinhard Furrer. Modelling temporally evolving and spatially globally dependent data. *Int. Stat. Rev.*, 86(2):344–377, 2018.

[28] Emilio Porcu, Moreno Bevilacqua, and Marc G. Genton. Spatio-temporal covariance and cross-covariance functions of the great circle distance on a sphere. *J. Amer. Statist. Assoc.*, 111(514):888–898, 2016.

[29] A. Quarteroni, R. Sacco, and F. Saleri. *Matematica Numerica*. Springer-Verlag Italia, Milan, 1998.

[30] Gabriel JE Rinkel, Mamuka Djibuti, Ale Algra, and J Van Gijn. Prevalence and risk of rupture of intracranial aneurysms: a systematic review. *Stroke*, 29(1):251–256, 1998.

[31] Laura M. Sangalli. Spatial regression with partial differential equation regularization. *International Statistical Review*, 2021.

[32] Laura M. Sangalli, James O. Ramsay, and Timothy O. Ramsay. Spatial spline regression models. *J. R. Stat. Soc. Ser. B. Stat. Methodol.*, 75(4):681–703, 2013.

[33] Vidar Thomée. *Galerkin finite element methods for parabolic problems*, volume 25 of *Springer Series in Computational Mathematics*. Springer-Verlag, Berlin, 2006.

[34] Grace Wahba. Spline interpolation and smoothing on the sphere. *SIAM J. Sci. Statist. Comput.*, 2(1):5–16, 1981.

[35] Matthieu Wilhelm, Luca Dedè, Laura M. Sangalli, and Pierre Wilhelm. IGS: an IsoGeometric approach for smoothing on surfaces. *Comput. Methods Appl. Mech. Engrg.*, 302:70–89, 2016.

[36] Keith J Worsley, Chien Heng Liao, John Aston, V Petre, GH Duncan, F Morales, and AC Evans. A general statistical analysis for fmri data. *Neuroimage*, 15(1):1–15, 2002.

MOX Technical Reports, last issues

Dipartimento di Matematica
Politecnico di Milano, Via Bonardi 9 - 20133 Milano (Italy)

74/2021 Orlando,G.; Barbante, P. F.; Bonaventura, L.
An efficient IMEX-DG solver for the compressible Navier-Stokes equations with a general equation of state

75/2021 Cicci, L.; Fresca, S.; Pagani, S.; Manzoni, A.; Quarteroni, A.
Projection-based reduced order models for parameterized nonlinear time-dependent problems arising in cardiac mechanics

73/2021 Marcinno, F.; Zingaro, A.; Fumagalli, I.; Dede', L.; Vergara, C.
A computational study of blood flow dynamics in the pulmonary arteries

71/2021 Franco, N.; Manzoni, A.; Zunino, P.
A Deep Learning approach to Reduced Order Modelling of parameter dependent Partial Differential Equations

72/2021 Fresca, S.; Manzoni, A.
POD-DL-ROM: enhancing deep learning-based reduced order models for nonlinear parametrized PDEs by proper orthogonal decomposition

70/2021 Beirao da Veiga, L.; Canuto, C.; Nochetto, R.H.; Vacca, G.; Verani, M.
Adaptive VEM: Stabilization-Free A Posteriori Error Analysis

69/2021 Antonietti, P.F.; Caldana, M.; Dede', L.
Accelerating Algebraic Multigrid Methods via Artificial Neural Networks

65/2021 Mazzieri, I.; Muhr, M.; Stupazzini, M.; Wohlmuth, B.
Elasto-acoustic modelling and simulation for the seismic response of structures: The case of the Tahtali dam in the 2020 Izmir earthquake

67/2021 Salvador, M.; Regazzoni, F.; Pagani, S.; Dede', L.; Trayanova, N.; Quarteroni, A.
The role of mechano-electric feedbacks and hemodynamic coupling in scar-related ventricular tachycardia

68/2021 Regazzoni, F.; Salvador, M.; Dede', L.; Quarteroni, A.
A machine learning method for real-time numerical simulations of cardiac electromechanics